Piezotronic Effect in Strain-Gated Transistor of *a*-Axis GaN Nanobelt

Ruomeng Yu,[†,#] Xingfu Wang,[†,#] Wenbo Peng,[†,#] Wenzhuo Wu,[†] Yong Ding,[†] Shuti Li,[*,§] and Zhong Lin Wang[*,†,‡]

[†]School of Materials Science and Engineering, Georgia Institute of Technology, Atlanta, Georgia 30332-0245, United States, [‡]Beijing Institute of Nanoenergy and Nanosystems, Chinese Academy of Sciences, 100083 Beijing, China, and [§]Guangdong Engineering Research Center of Optoelectronic Functional Materials and Devices, Institute of Opto-Electronic Materials and Technology, South China Normal University, 510631 Guangzhou, China. [#]R.Y., X.W., and W.P. contributed equally to this work.

ABSTRACT Due to the non-centrosymmetric crystal structures, wurtzite family semiconducting materials possess piezoelectric properties and exhibit polarizations along certain directions upon straining. Utilizing strain-induced piezoelectric polarization charges to modulate the energy band structures and thus to tune/control the transport processes of charge carriers is referred to as the piezotronic effect. Distinct from the previous studies of *c*-axis GaN nanowires, here we systematically study the piezotronic-effect-induced mod-

ifications of energy band structures and the corresponding influence on electronic transport properties of *a*-axis GaN nanobelts. The physical mechanism is carefully illustrated and further confirmed by theoretical simulations *via* finite element analysis. The spatial distributions of local carrier concentration and the energy band diagrams of *a*-axis GaN under various straining conditions are calculated. This work provides a thorough understanding of strain-gated transport properties of *a*-axis GaN piezotronic transistors and its future applications in semiconductor devices.
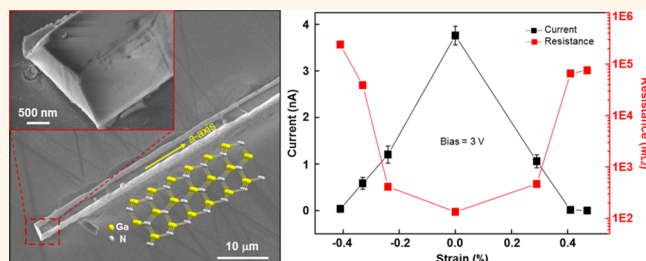
KEYWORDS: piezotronic effect · *a*-axis · GaN · transistor · strain-gated

Under mechanical deformations along certain crystal orientations, wurtzite family materials with non-centrosymmetric crystal structures undergo relative displacements between the centers of positive and negative ions, leading to polarizations known as the piezoelectric effect, which has been widely used in electromechanical sensing,[1−3] actuation,[4,5] and energy harvesting.[6−8] Conventional piezoelectric materials such as $Pb(Zr_xTi_{1−x})O_3$ (PZT) and polyvinylidene fluoride (PVDF) are insulators and may not be applicable for constructing functional electronics. The effect of mechanically induced polarization on electronic transport processes of charge carriers in piezoelectric materials has therefore been long overlooked. Recently, the two-way coupling between piezoelectric polarization and semiconductor properties in wurtzite-structured piezoelectric semiconductors, such as ZnO and GaN, has resulted in both novel fundamental phenomena[9−11] and unprecedented device characteristics as well as applications,[12−14] leading to increasing research interests in

an emerging field of piezotronics. For semiconductor materials lacking inversion symmetry, piezoelectric polarization charges created upon straining can modulate the energy band structures and thus tune/control the transport processes of charge carriers. This is the piezotronic effect.[15] However, all of the previous reports merely investigated nanostructures synthesized along the *c*-axis direction for both fundamental study[10,11] and various applications,[12−14] and it remains unclear how the piezotronic effect affects the transport properties of *a*-axis-oriented wurtzite family semiconducting nanostructures.

In this work, by using the GaN nanobelts synthesized along the *a*-axis direction, the corresponding piezotronic effect is studied by measuring the electronic transport properties of single-nanobelt transistors. The physical mechanism is carefully illustrated and further confirmed by theoretical simulations *via* finite element analysis (FEA). Theoretical calculations are also conducted to reveal the spatial distributions of local carrier concentrations and the energy band

diagrams of *a*-axis-oriented GaN nanobelts under different straining conditions. This work systematically analyzes the transport properties of strain-gated transistors (SGTs) based on *a*-axis-oriented GaN nanobelts, and the results provide a fundamental understanding about the piezotronic effect along different crystal orientations, which can be useful for semiconductor-based electronics for logic computations, sensing systems, human—machine interfacing, implantable surgical instruments, and biomedical diagnostics.[16−20]

RESULTS AND DISCUSSION

Patterned silicon substrates used for GaN growth are fabricated by photolithography and wet chemical etching to form 800 nm deep trapezoidal grooves with two opposed Si(111) facets separated by a bottom Si(100) facet. GaN nanobelts are then synthesized on the patterned Si(100) substrate in a metal—organic chemical vapor deposition reactor under 1050 °C and 400 mbar for 1800 s. Detailed synthesizing processes are found in Methods.[21] The morphology of the as-synthesized GaN nanobelts is characterized by scanning electron microscopy (SEM), as presented in Figure 1a, clearly showing a trapezoidal cross section as the inset with a height of 1 μm, a width of 2 μm, and a length of 100−200 μm. High-resolution transmission electron microscopy (HRTEM) images and the corresponding

selected area electron diffraction (SAED) patterns presented in Figure 1b provide more insight on the as-synthesized GaN nanobelts. Single-crystal GaN is achieved as shown in Figure 1b1,b3. The growth orientation is perpendicular to the normal directions of planes $(0\bar{1}11)$ and $(0\bar{1}12)$, as indicated by the SAED patterns in Figure 1b2,b4. Therefore, it is confirmed that the GaN nanobelts used in this work are synthesized along the $\langle 2\bar{1}\bar{1}0 \rangle$ direction (*i.e.*, *a*-axis-oriented growth). The SGTs are fabricated by applying silver paste at both ends of the GaN nanobelt as source and drain electrodes. Detailed fabrication processes are found in Methods.

The physical mechanism of the piezotronic effect on electronic transport properties of *a*-axis GaN nanobelt SGTs under mechanical strains is investigated and schematically illustrated in Figure 1c—e. Motions of charge carriers under different straining conditions are depicted in the bottom panels (Figure 1c—e), while the corresponding piezoelectric potential distributions are theoretically simulated *via* FEA and presented in the top panels (Figure 1c—e). As an n-type semiconductor with donor concentration $N_D = 2 \times 10^{17}$ cm^{-3}, the as-synthesized *a*-axis GaN nanobelt presents electrons as majority charge carriers (Figure 1c, bottom) without piezo-potential distribution (Figure 1c, top) under strain-free conditions, as shown in Figure 1c.
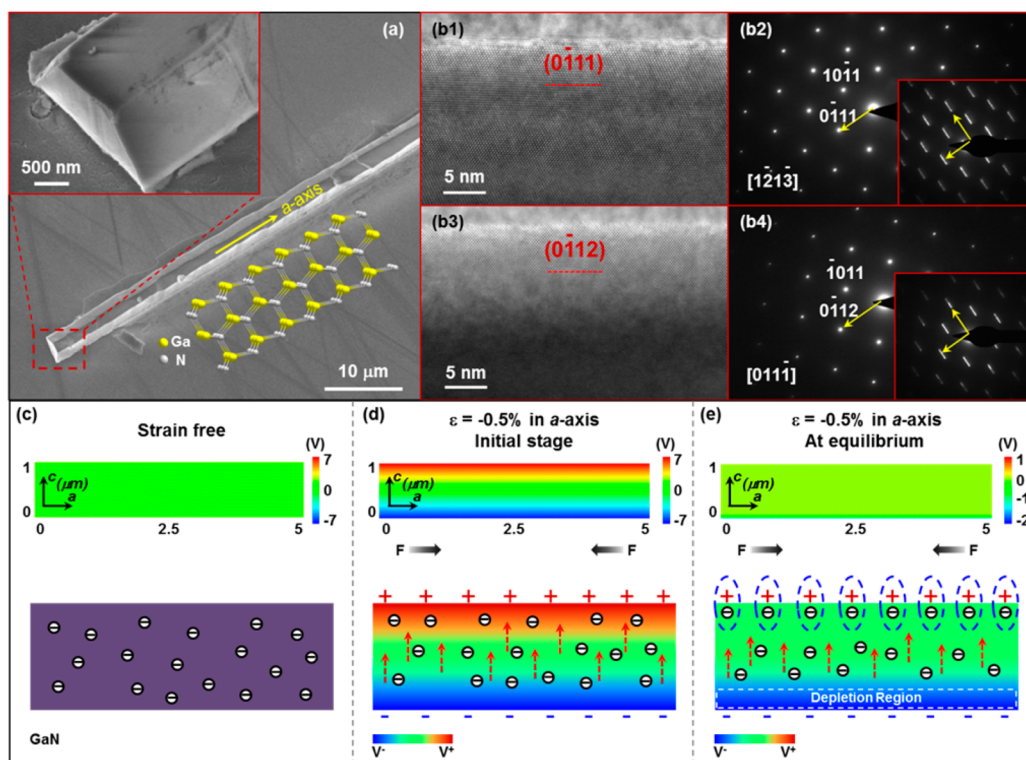

Figure 1. Characterizations and working mechanism of GaN nanobelt SGTs. (a) SEM images of the as-synthesized GaN nanobelt with trapezoidal cross section as the inset. **(b)** HRTEM images (b1,b3) and the corresponding SAED patterns (b2,b4) of GaN nanobelts. **(c−e)** Schematic illustration of the working mechanism of GaN nanobelt SGTs **(c)** under strain-free condition, **(d)** with −0.5% compressive strains applied at the initial stage, **(e)** under −0.5% compressive strains at equilibrium. Top panels: FEA simulations of piezoelectric potential distributions. Bottom panels: Schematic illustration of carriers' motions.

By applying a compressive strain $\varepsilon = -0.5\%$ along the a-axis direction (Figure 1d), at the initial stage, an instantaneous piezo-potential distribution is produced (Figure 1d, top) with positive piezoelectric polarization charges at the $+c$ plane and negative piezo-charges at the $-c$ plane (Figure 1d, top). Thus, mobile electrons are repelled by negative piezo-charges toward the $+c$ plane, as shown in the bottom panel of Figure 1d. At equilibrium, most of the positive piezoelectric polarization charges at the $+c$ plane are screened by mobile electrons,[22] while an electron depletion region is generated near negative piezo-charges at the $-c$ plane, as schematically shown in the bottom panel of Figure 1e. The corresponding piezo-potential distributions are calculated and presented in the top panel of Figure 1e. Considering the symmetric configuration of GaN nanobelt SGTs with respect to the a-axis, similar carrier motions and piezo-potential distributions are expected for tensile strain (along a-axis) scenarios, with electron depletion region induced at the $+c$ plane and positive piezo-charges screened by electrons at the $-c$ plane. Therefore, externally applied compressive/tensile strains tune/control the transport properties of a-axis GaN nanobelt SGTs as the gate by forming an electron depletion region to shrink the conducting channel and thus increase the resistance of the GaN nanobelts. This working mechanism is fundamentally new in physics and different from that in c-axis piezoelectric nanostructures, whose electric transport is determined by the asymmetric changes of barrier height at both Schottky contacts of the two-terminal devices.[10]

Meanwhile, two Schottky barriers are formed between GaN and Ag when applying silver paste at both ends of the nanobelt for source and drain electrodes.[10] Upon compressive/tensile straining, negative piezoelectric polarization charges (Figure 1e) are presented at the local GaN/Ag interface after equilibrium; positive piezo-charges are screened by mobile carriers (Figure S1, Supporting Information). The barrier heights at both Schottky contacts are therefore increased by negative piezo-charges and thus hinder the transport of electrons across the local energy barrier (Figure S1), which is equivalent to increasing the resistance of GaN nanobelt-based transistors. Therefore, as more compressive/tensile strains are applied, the resistance of GaN nanobelt-based transistors is increased due to the formation of the electron depletion region and the increased Schottky barrier height (SBH).

Piezotronic effect on the transport properties of a-axis GaN nanobelt SGTs is systematically studied by applying different bias voltages on the devices under various straining conditions. The experimental setups and the optical images of the as-fabricated GaN nanobelt SGTs are presented in Figure 3a. Details about applying strains and calculating the strain values are illustrated in Methods. $I-V$ characteristics of GaN nanobelt SGTs under a series of compressive and tensile strains are measured and summarized in Figure 2a,b, respectively, by applying a triangular wave ranging from -3 V to $+3$ V. Obviously, the output currents of GaN nanobelt SGTs decrease as increasing compressive/tensile strains. The pseudo-transconductance $g_\mathrm{m} = (|dI|/d\varepsilon_\mathrm{g})$ at a bias voltage of 3 V is derived by calculating the current differences per unit strain between strain-free and certain straining conditions of the devices. The results are presented as insets in Figure 2a,b, indicating the gating effect of externally applied strains over the transport properties and output currents of a-axis GaN nanobelt SGTs. The maximum value of g_m is obtained under 0.29% tensile strain with the value of $g_\mathrm{m} = 12.9$ (μA/$\Delta\varepsilon_\mathrm{g}$%), at a bias voltage of 7 V (Figure 2e). Changes of current are plotted as a function of applied strains at a bias voltage of 3 V (Figure 2c, black), while the corresponding resistance changes are calculated (Methods) and displayed in Figure 2c as red symbols. Obviously, the current decreases and the resistance increases by applying more compressive/tensile strains, which is distinguishable from the asymmetric changes of currents/resistances observed in c-axis nanostructures upon compressive and tensile straining[10] due to the different working mechanisms.

Based on the fact that the resistance of a-axis GaN nanobelts increases by applying both compressive and tensile strains, the electronic transport properties of GaN under strains are dominated by the piezotronic effect instead of the piezoresistive effect. The piezoresistive effect is defined as $\Delta R/R = \pi\sigma$ (R is the resistance, π is the piezoresistive coefficient, σ is the stress), and the changes of resistance are inverse under compressive and tensile strains. Furthermore, the piezoresistive coefficient π is calculated by extracting the data at 3 V biased voltage (Figure 2a), with relative changes of resistance between unstrained and -0.41% compressively strained conditions, $\Delta R/R = 73.2$ and stress $\sigma = \varepsilon \times E$ ($E = 181$ GPa is the Young's modulus of GaN). The calculated π is on the order of 1×10^{-7} Pa^{-1}, which is 3 orders in magnitude larger than the typical value at the 10^{-10} level.[23] This result further confirms that it is the piezotronic effect, rather than the piezoresistive effect, that plays an essential role in controlling the electronic transport properties of a-axial GaN nanobelt SGTs. More experimental measurements are conducted under 5 V (Figure S2) and 7 V (Figure 2d$-$f) biased voltages; similar performances are obtained under different straining conditions for both investigations. All the observed results indicate the increasing resistance and decreasing current under stronger compressive/tensile strains, as predicted by the proposed working mechanism. Over 50 devices are measured during the experiments, most of which possess similar electronic transport properties as described above, indicating the reliability and reproducibility of these results.
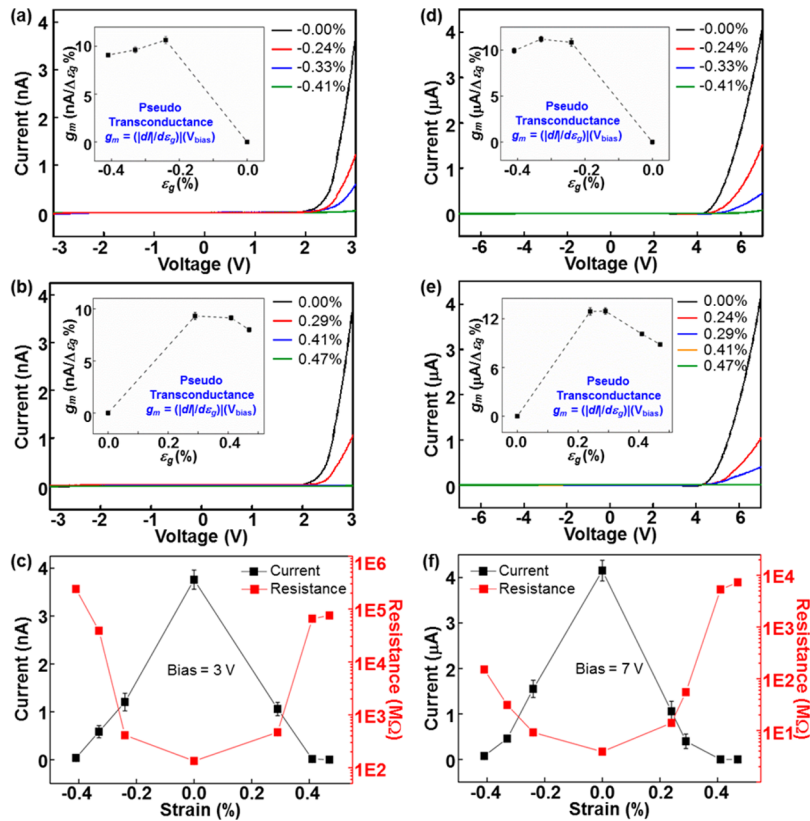
Figure 2. Piezotronic effect on *I*−*V* characteristics of *a*-axis GaN nanobelt SGTs. (a,b) *I*−*V* characteristics of GaN nanobelt SGTs under a series of (a) compressive and (b) tensile strains under triangular wave ranging from −3 V to +3 V. The insets are the corresponding pseudo-transconductance at 3 V. (c) Current and resistance response to strains at a bias voltage of 3 V. (d,e) *I*−*V* characteristics of GaN SGTs under a series of (d) compressive and (e) tensile strains under triangular wave ranging from −7 V to +7 V. The insets are the corresponding pseudo-transconductance at 7 V. (f) Current and resistance response to strains at a bias voltage of 7 V.

Theoretical calculations are performed to obtain insight on the modifications of energy band structure and charge carrier distributions by the piezotronic effect. Upon straining, charge carriers redistribute within GaN due to the electric field established by strain-induced piezoelectric polarization charges. The mechanical equilibrium and the direct piezoelectric effect are expressed as[22]

$$\begin{cases} \sigma_p = c_{pq}\varepsilon_q - e_{pk}E_k \\ D_i = e_{iq}\varepsilon_q + \kappa_{ik}E_k \end{cases} \quad (1)$$

where σ is the stress tensor, ε is the strain tensor, E is the electric field, D is the electric displacement, c_{pq} is the mechanical stiffness tensor, e_{pk} and e_{iq} are the piezoelectric constant, and κ_{ik} is the dielectric constant. The Voigt−Nye notation is used. By substituting the second equation into Gauss's law, the equation for the electric field is derived:

$$\nabla \cdot D = \frac{\partial}{\partial x_i}(e_{iq}\varepsilon_q + \kappa_{ik}E_k) = \rho$$

$$= e(p - n + N_D^+ - N_A^-) \quad (2)$$

where p is the hole concentration in the valence band, n is the electron concentration in the conduction band,

N_D^+ is the ionized donor concentration, and N_A^- is the ionized acceptor concentration. $p = N_A^- = 0$ is adopted for n-type GaN nanobelts used in this work. Therefore, eq 2 transfers into

$$\nabla \cdot D = \frac{\partial}{\partial x_i}(e_{iq}\varepsilon_q + \kappa_{ik}E_k) = \rho = e(-n + N_D^+) \quad (3)$$

The redistribution of electrons under thermodynamic equilibrium is given by the Fermi−Dirac statistics

$$\begin{cases} n = N_c \dfrac{2}{\sqrt{\pi}} \displaystyle\int_{E_c(x)}^{\infty} \dfrac{[(E - E_c(x))/kT]^{1/2}\ dE}{1 + \exp[(E - E_F)/kT]kT} \\ N_c = 2\left(\dfrac{2\pi m_e kT}{h^2}\right)^{3/2} \end{cases} \quad (4)$$

where the conduction band edge $E_c(x)$ is a function of space coordinates. N_c, the effective state density of conduction band, is determined by the effective mass of conduction band electrons m_e and temperature T. Considering the obvious mechanical deformation, the band edge shift ΔE_c is the sum of the electrostatic energy part and the deformation potential part

$$\Delta E_c = E_c - E_{c0} = -e\varphi + \Delta E_c^{deform}$$
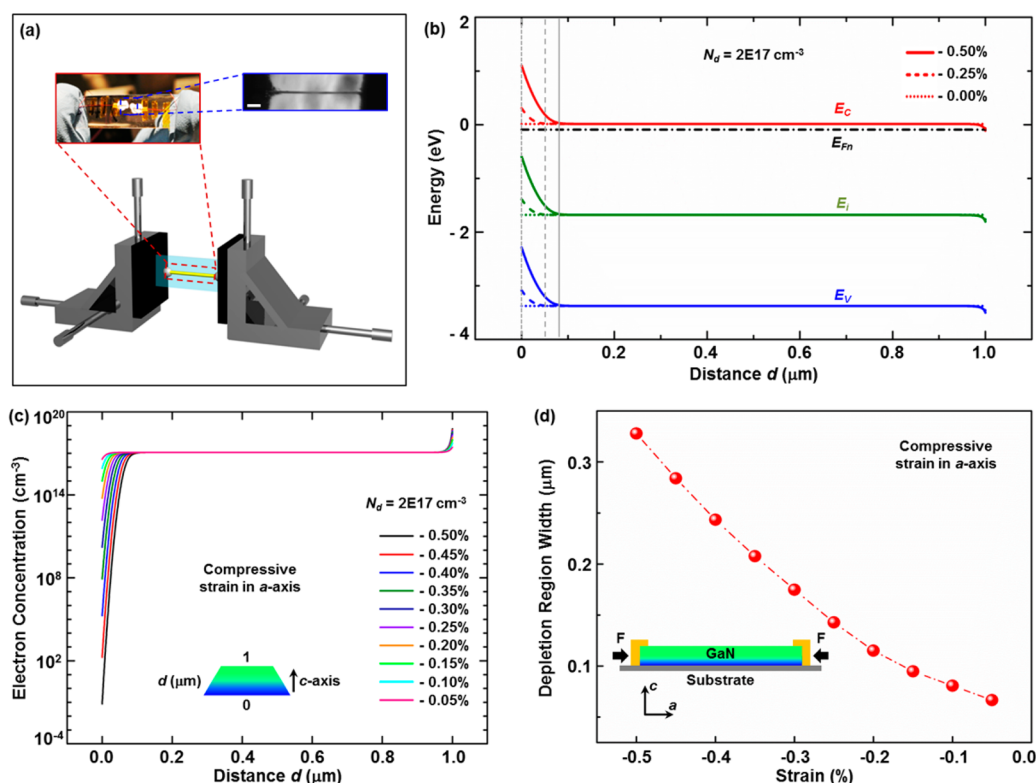
$$= -e\varphi + a_c\frac{\Delta V}{V} \quad (5)$$

Figure 3. Theoretical simulations under compressive strains. (a) Experimental setup and optical images of GaN nanobelt SGTs. Scale bar is 50 μm. **(b)** Energy band diagram of GaN SGTs under 0% (short dotted line), −0.25% (short dashed line), and −0.50% (solid line) compressive strains. **(c)** Spatial distribution of local electron concentrations along the *c*-axis within GaN under different compressive straining conditions. Donor concentration is $N_D = 2 \times 10^{17}$ cm^{-3}. **(d)** Width of electron depletion region under different compressive strains along the *a*-axis.

where E_{c0} is the conduction band edge of a freestanding unstrained GaN nanobelt; $\Delta E_c^{deform} = a_c \Delta V/V$ is the band edge shift due to the deformation potential, which is proportional to the relative volume change $\Delta V/V$, and a_c is the deformation potential constant. Finally, the activation process of the donors is given by

$$N_D^+ = N_D \frac{1}{1 + 2\exp\left(\dfrac{E_F - E_D(x)}{kT}\right)} \qquad (6)$$

where $E_D(x) = E_c(x) - \Delta E_D$ is the position-dependent donor energy level. The constant ΔE_D is the activation energy of the donors.

With nonlinear partial differential eqs 1−6 solved by FEA, the piezoelectric potential distributions (Figure 1c−e, top), energy band diagrams (Figure 3b), and local carrier concentrations (Figure 3c) in a GaN nanobelt under mechanical strains along *a*-axis direction are derived. Detailed simulation parameters and FEA simulation process are found in Supporting Information (part C). Figure 3c displays the spatial distribution of electron concentrations along the *c*-axis direction under a series of compressive straining conditions. Energy band diagrams of GaN under 0% (Figure 3b, short dotted line), −0.25% (Figure 3b, short dashed line), and −0.50% (Figure 3b, solid line) compressive strains are shown in Figure 3b, indicating different

bending positions of the energy band edge. More energy band diagrams under other compressive strains are calculated and shown in Figure S3 (Supporting Information). Depletion region width is determined by locating the bending position of the energy band edge[24] and plotted as a function of compressive strains, as shown in Figure 3d. It is clear that a wider electron depletion region is achieved under stronger compressive strains, which agrees well with experimental results and the proposed physical mechanism. Also, it rules out the role played by the piezoresistive effect in the measured transport characteristics. Same calculations are conducted for tensile strain (along *a*-axis) situations, as shown in Figure S4 (Supporting Information). Due to the symmetric configuration of GaN nanobelt SGTs, the same behaviors are observed for energy band diagrams (Figure S4b) and local electron concentrations (Figure S4a) with opposite spatial distributions. The width of the electron depletion region also increases as more tensile strains are applied (Figure S4c).

The dominate role played by the piezotronic effect in tuning/controlling the electronic transport processes of GaN nanobelt SGTs under mechanical strains is further confirmed by conducting control experiments to apply compressive strains along the *c*-axis of the GaN nanobelt (Figure 4). Under strain-free conditions,
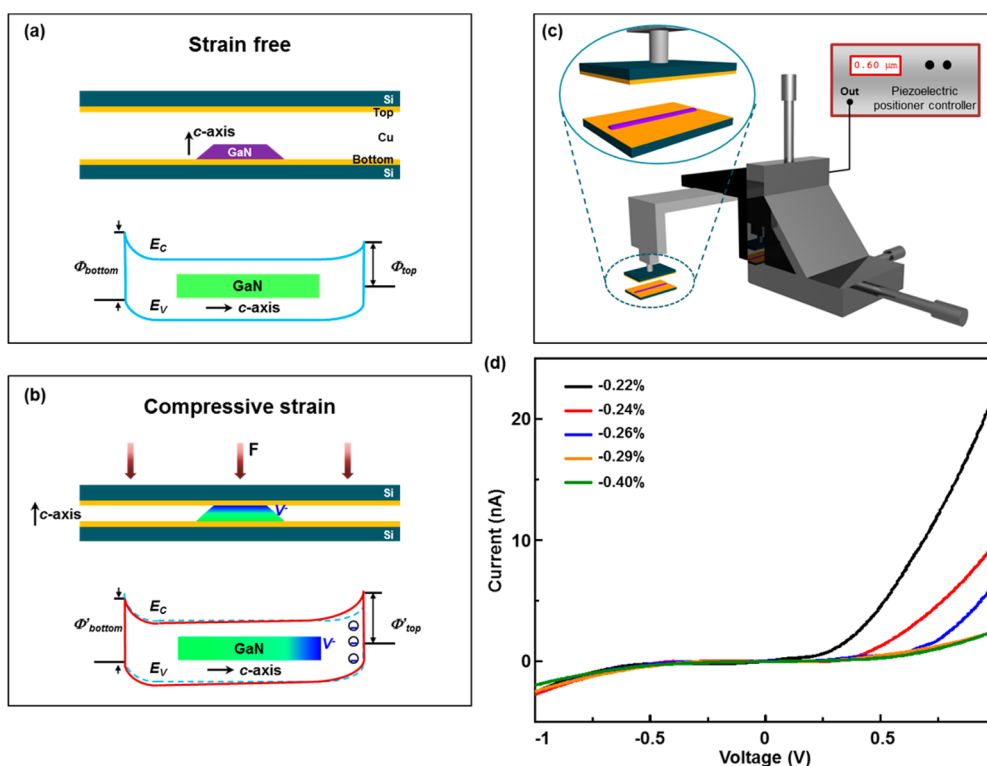
Figure 4. *I−V* characteristics of GaN nanobelt SGTs under *c*-axis strains. (a,b) Experimental setup and the corresponding energy band diagram of GaN SGTs under (a) strain-free condition and (b) compressive strains along the *c*-axis. (c) Experimental setup of the *c*-axis strain measurements. (d) *I−V* characteristics of GaN SGTs under various compressive strains along the *c*-axis. Note: The current flow is along the *c*-axis.

the GaN nanobelt is placed on the bottom Si wafer (1 cm by 1 cm) coated by copper as an electrode, with its *c*-axis pointing upward (Figure 4a). Another copper-coated Si wafer (1 cm by 1 cm) is attached to a piezo-electric positioner (movement resolution ∼10 nm), as shown in Figure 4c, to apply compressive strains and serves as the top electrode, as well. By pressing down the top Si wafer, compressive strains are applied on the GaN nanobelt along its *c*-axis orientation (Figure 4b). The corresponding energy band diagram is sche-matically presented in Figure 4b, with the SBH between GaN and the top electrode increasing, while the SBH between GaN and the bottom electrode remains unchanged because negative piezoelectric polariza-tion charges are present at the +*c* plane and positive piezo-charges are screened by mobile electrons, and no obvious piezoelectric potential is observed at the −*c* plane. These energy band diagrams perfectly explain the obtained *I−V* characteristics of GaN nano-belt SGTs, as shown in Figure 4d: output currents measured along the *c*-axis at +1 V biased voltage decrease as the applied strains are increased since the barrier height of the corresponding reversely biased Schottky contact is increased, whereas the currents at −1 V remain unchanged because the barrier height of the corresponding reversely biased Schottky contact is unchanged due to the screening effect. Details about applying strains in the *c*-axis

direction and calculating the strain values are de-scribed in Methods.

CONCLUSIONS

Different from previous reports that focus on the fundamental study and applications of the piezotronic effect on nanostructures grown along the *c*-axis, *a*-axis GaN nanobelts are synthesized and fabricated as SGTs in this work. The piezotronic effect on the modifica-tions of energy band structures and the corresponding electronic transport properties of GaN nanobelt SGTs are systematically investigated. *I−V* characteristics of GaN nanobelt SGTs are measured under different bias voltages and straining conditions. Upon stronger com-pressive/tensile straining, the resistance of GaN nano-belts is increased and the currents of SGTs are decreased by the piezotronic effect. Wider electron depletion region and increased SBH induced by more mechanical strains are accounted for by the obtained electronic transport behaviors. Theoretical calcula-tions/simulations *via* FEA are conducted to provide insight into the physical mechanism of the piezotronic effect. The spatial distributions of local carrier concen-tration along the *c*-axis and the energy band diagrams of the *a*-axis GaN nanobelts under different straining conditions are presented to support the proposed working mechanism. This work systematically investi-gates the electronic transport behaviors of *a*-axis GaN

METHODS

Synthesizing GaN Nanobelts. First, a 100 nm thick SiO_2 film is deposited on Si(100) substrates by plasma-enhanced chemical vapor deposition. Second, periodic stripes (5 μm spacing, 5 μm width) of SiO_2 along the $\langle 11\bar{2}0 \rangle$ direction are formed by photolithography and wet chemical etching. Third, 800 nm deep trapezoidal grooves with two opposed Si(111) facets separated by a bottom Si(100) facet are fabricated through anisotropic etching by immersing the substrates in a KOH solution (30 wt %) at 40 °C for 20 min. Prior to growth, the substrates are immersed in HF (7%) to yield an oxide-free hydrogen-passivated Si surface, followed by cleaning with deionized water. Finally, the patterned Si(100) substrate is loaded into a metal−organic chemical vapor deposition reactor (Thomas Swan Scientific Equipment Ltd.) for epitaxial growth of GaN. Trimethylgallium (TMG), trimethylaluminum (TMAl), and ammonia (NH_3) are used as Ga, Al, and N sources, respectively. A 30 nm AlN interlayer is selectively grown on the two opposite Si(111) facets at first, then GaN nanobelts are synthesized under 1050 °C and 400 mbar in hydrogen for 1800 s using TMG (50 sccm) and NH_3 (5000 sccm).

Materials Characterization. Detailed microscopic structures of GaN nanobelts are characterized by scanning electron microscope (Hitachi SU8010), transmission electron microscope (Tecnai G2) with SAED, and HRTEM (FEI F30).

Device Fabrication Process. The device is fabricated by transferring and bonding an individual GaN nanobelt laterally on a polyethylene terephthalate substrate with its a-axis in the plane of the substrate. Silver paste is applied to fix both ends of the nanobelt and serve as source and drain electrodes. A thin layer of polydimethylsiloxane is used to package the device for enhancing its robustness as well as protecting it from possible corrosion or contamination in the environment.

External Strain Calculations. External strains along the a-axis are applied on GaN nanobelt SGTs by locking the device between two 3D mechanical stages (moving resolution ∼10 μm) facing each other, as shown in Figure 3a. By moving two 3D stages toward each other, a compressive or tensile strain is applied on the devices. The value of strain applied on the device is calculated following the method reported previously by Yang et al.[25]

External strains along the c-axis are applied on GaN by pressing the nanobelt placed on a copper-coated bottom Si wafer (1 cm by 1 cm, Figure 4) in the c-axis direction through a copper-coated top Si wafer (1 cm by 1 cm, Figure 4) attached to the piezoelectric positioner (movement resolution ∼10 nm) via a layer of double-sided kapton polyimide tape with the thickness of 100 μm (consisting of 25 μm kapton film and 75 μm silicone adhesive layer). Considering that the Young's modulus of silicone is 0.01 GPa (obtained from the manufacturer), which is much smaller than that of other materials (kapton ∼2.5 GPa, Si ∼150 GPa, GaN ∼181 GPa) stacked in the measurement setup, when applying a certain compressive force on the system, most of the deformation is produced in the silicone layers. Under the condition of static mechanic equilibrium, the forces are uniformly distributed in different materials, and then the strain in GaN nanobelts is calculated based on the Young's modulus ratio among the materials,[26] as labeled in Figure 4d.

Measurements. A function generator (model no. DS345, Stanford Research Systems, Inc.), a low-noise voltage preamplifier (model no. SR560, Stanford Research Systems, Inc.), and a low-noise current preamplifier (model no. SR570, Stanford Research Systems, Inc.) in conjunction with a GPIB controller (GPIB-USB-HS, NI 488.2) are used for electrical measurements. Computer-controlled measurement software is used to collect and record the data.

Resistance Calculations. The resistances of GaN nanobelt SGTs are calculated by fitting the measured I−V characteristics with a Matlab-based GUI program "PKUMSM" developed by Peng et al.,[27] and the detailed theoretical models of the Matlab program are found in the previous report.[27]

Conflict of Interest: The authors declare no competing financial interest.

Supporting Information Available: The Supporting Information is available free of charge on the ACS Publications website at DOI: 10.1021/acsnano.5b02817.

More information about the physical mechanism; I−V characteristics under 5 V biased voltage and various strains; energy band diagrams of GaN under various compressive strains; spatial distribution of local electron concentrations, energy band diagrams, and the width of the electron depletion region of GaN under various tensile strains (PDF)

REFERENCES AND NOTES

1. Muramatsu, H.; Suda, M.; Ataka, T.; Seki, A.; Tamiya, E.; Karube, I. Piezoelectric Resonator as a Chemical and Biochemical Sensing Device. *Sens. Actuators, A* **1990**, *21*, 362–368.
2. Qiu, Y.; Buttry, D. A. Strategies for Chemical Sensing in Liquids with Piezoelectric Quartz Crystal Microbalances. *Abstr. Pap. Am. Chem. S* **1991**, *201*, 19-Afgd.
3. Hagood, N. W.; Anderson, E. H. Simultaneous Sensing and Actuation Using Piezoelectric Materials. *Proc. SPIE* **1991**, *1543*, 409–421.
4. Newton, D.; Main, J.; Garcia, E.; Massengill, L. Piezoelectric Actuation Systems: Optimization of Driving Electronics. *Proc. SPIE* **1996**, *2717*, 259–266.
5. Kusakabe, C.; Tomikawa, Y.; Takano, T. High-Speed Actuation of a Piezoelectric Actuator by Pulse Driving and Stopping of Its Residual Mechanical Vibration. *Ieee T Ultrason Ferr* **1990**, *37*, 551–557.
6. Wang, Z. L.; Song, J. H. Piezoelectric Nanogenerators Based on Zinc Oxide Nanowire Arrays. *Science* **2006**, *312*, 242–246.
7. Wang, X. D.; Song, J. H.; Liu, J.; Wang, Z. L. Direct-Current Nanogenerator Driven by Ultrasonic Waves. *Science* **2007**, *316*, 102–105.
8. Qin, Y.; Wang, X. D.; Wang, Z. L. Microfibre-Nanowire Hybrid Structure for Energy Scavenging. *Nature* **2008**, *451*, 809–813.
9. Wang, Z. L. Nanopiezotronics. *Adv. Mater.* **2007**, *19*, 889–892.
10. Yu, R. M.; Dong, L.; Pan, C. F.; Niu, S. M.; Liu, H. F.; Liu, W.; Chua, S.; Chi, D. Z.; Wang, Z. L. Piezotronic Effect on the Transport Properties of GaN Nanobelts for Active Flexible Electronics. *Adv. Mater.* **2012**, *24*, 3532–3537.
11. Wu, W. Z.; Wang, L.; Li, Y. L.; Zhang, F.; Lin, L.; Niu, S. M.; Chenet, D.; Zhang, X.; Hao, Y. F.; Heinz, T. F.; Hone, J.; Wang, Z. L. Piezoelectricity of Single-Atomic-Layer MoS2 for Energy Conversion and Piezotronics. *Nature* **2014**, *514*, 470–474.
12. Wu, W. Z.; Wen, X. N.; Wang, Z. L. Taxel-Addressable Matrix of Vertical-Nanowire Piezotronic Transistors for Active and Adaptive Tactile Imaging. *Science* **2013**, *340*, 952–957.
13. Yu, R. M.; Pan, C. F.; Chen, J.; Zhu, G.; Wang, Z. L. Enhanced Performance of a ZnO Nanowire-Based Self-Powered Glucose Sensor by Piezotronic Effect. *Adv. Funct. Mater.* **2013**, *23*, 5868–5874.

nanobelt SGTs controlled by piezotronic effect and provides guidance to potential applications of piezotronic effect on semiconductor-based electronic devices for logic computations, sensing systems, human−machine interfacing, implantable surgical instruments, and biomedical diagnostics.

14. Zhou, J.; Gu, Y. D.; Fei, P.; Mai, W. J.; Gao, Y. F.; Yang, R. S.; Bao, G.; Wang, Z. L. Flexible Piezotronic Strain Sensor. *Nano Lett.* **2008**, *8*, 3035–3040.

15. Wang, Z. L. Piezotronic and Piezophototronic Effects. *J. Phys. Chem. Lett.* **2010**, *1*, 1388–1393.

16. Santhanam, G.; Ryu, S. I.; Yu, B. M.; Afshar, A.; Shenoy, K. V. A High-Performance Brain-Computer Interface. *Nature* **2006**, *442*, 195–198.

17. Wang, C.; Hwang, D.; Yu, Z. B.; Takei, K.; Park, J.; Chen, T.; Ma, B. W.; Javey, A. User-Interactive Electronic Skin for Instantaneous Pressure Visualization. *Nat. Mater.* **2013**, *12*, 899–904.

18. Tee, B. C. K.; Wang, C.; Allen, R.; Bao, Z. N. An Electrically and Mechanically Self-Healing Composite with Pressure- and Flexion-Sensitive Properties for Electronic Skin Applications. *Nat. Nanotechnol.* **2012**, *7*, 825–832.

19. Tian, B. Z.; Liu, J.; Dvir, T.; Jin, L. H.; Tsui, J. H.; Qing, Q.; Suo, Z. G.; Langer, R.; Kohane, D. S.; Lieber, C. M. Macroporous Nanowire Nanoelectronic Scaffolds for Synthetic Tissues. *Nat. Mater.* **2012**, *11*, 986–994.

20. Kaltenbrunner, M.; Sekitani, T.; Reeder, J.; Yokota, T.; Kuribara, K.; Tokuhara, T.; Drack, M.; Schwodiauer, R.; Graz, I.; Bauer-Gogonea, S.; Bauer, S.; Someya, T. An Ultra-Lightweight Design for Imperceptible Plastic Electronics. *Nature* **2013**, *499*, 458–463.

21. Wang, X. F.; Tong, J. H.; Chen, X.; Zhao, B. J.; Ren, Z. W.; Li, D. W.; Zhuo, X. J.; Zhang, J.; Yi, H. X.; Liu, C.; Fang, F.; Li, S. T. Highly Ordered GaN-Based Nanowire Arrays Grown on Patterned (100) Silicon and Their Optical Poperties. *Chem. Commun.* **2014**, *50*, 682–684.

22. Gao, Y.; Wang, Z. L. Equilibrium Potential of Free Charge Carriers in a Bent Piezoelectric Semiconductive Nanowire. *Nano Lett.* **2009**, *9*, 1103–1110.

23. Peng, B. Mechanical Characterization of One-Dimensional Nanomaterials. Northwestern University, 2008.

24. Sze, S. M. *Physics of Semiconductor Devices*; John Wiley & Sons: New York, 1981.

25. Yang, R. S.; Qin, Y.; Dai, L. M.; Wang, Z. L. Power Generation with Laterally Packaged Piezoelectric Fine Wires. *Nat. Nanotechnol.* **2009**, *4*, 34–39.

26. Pan, C. F.; Dong, L.; Zhu, G.; Niu, S. M.; Yu, R. M.; Yang, Q.; Liu, Y.; Wang, Z. L. High-Resolution Electroluminescent Imaging of Pressure Distribution Using a Piezoelectric Nanowire LED Array. *Nat. Photonics* **2013**, *7*, 752–758.

27. Liu, Y.; Zhang, Z. Y.; Hu, Y. F.; Jin, C. H.; Peng, L. M. Quantitative Fitting of Nonlinear Current-Voltage Curves and Parameter Retrieval of Semiconducting Nanowire, Nanotube and Nanoribbon Devices. *J. Nanosci. Nanotechnol.* **2008**, *8*, 252–258.